Nanoscale Advances

ROYAL SOCIETY OF CHEMISTRY

PAPER

View Article Online
View Journal | View Issue

Cite this: *Nanoscale Adv.*, 2022, **4**, 173

pH-responsive hollow Fe–gallic acid coordination polymer for multimodal synergistic-therapy and MRI of cancer†

Congcong Liu,[a] Chengcheng Li,[a] Sen Jiang,[a] Cheng Zhang[b] and Yang Tian *[a]

Tumor-microenvironment (TME) responsive nanostructures are attractive for drug delivery in clinical cancer treatment. The coordination polymer Fe–gallic acid (Fe–GA) is one of the promising drug carriers due to its pH-response, good biocompatibility, and minimal side effects. However, the hollow nanostructures of Fe–GA have not been reported until now, which seriously limits the quantity of drug delivery. Herein, hollow Fe–GA nanospheres were prepared for the first time with bovine serum albumin (BSA) combination (denoted as Fe–GA/BSA) under mild reaction conditions. Then, the antitumor drug doxorubicin (DOX) was loaded in the hollow Fe–GA/BSA to obtain Fe–GA/BSA@DOX. A series of experiments *in vitro* and *in vivo* indicated that the Fe–GA/BSA@DOX could efficiently respond to TME and release DOX and Fe(III) ions. Furthermore, the Fe(III) could consume overexpressed glutathione (GSH) in cancer cells and generate Fe(II) to trigger the Fenton reaction, producing ·OH for chemodynamic treatment (CDT) of cancer. In addition, the Fe–GA/BSA@DOX could effectively convert near-infrared (NIR) light into heat by acting as a photothermal therapy (PTT) agent. Besides that, magnetic resonance imaging (MRI) data also showed that the Fe–GA/BSA had beneficial T_1 and T_2 imaging effects, demonstrating that the hollow Fe–GA/BSA has potential for multimodal synergistic cancer MRI diagnosis and therapies of drugs, CDT, and PTT.

Received 30th September 2021
Accepted 28th October 2021

DOI: 10.1039/d1na00721a

rsc.li/nanoscale-advances

1. Introduction

Cancer is still a severe threat to human health in the world. Drug treatment is regarded as one of the indispensable means in the clinic to face the cancer menace.[1,2] In recent years, drug delivery based on nanomaterials in cancer therapy has been attractive due to the controlled release, targeted delivery, and multiple-drug loading,[1,3–5] which can enhance the cancer cure rate and reduce side effects.[6] At present, general nanomaterials for drug delivery include inorganic nanoparticle drug binders,[7–9] organic polymers,[10,11] hydrogel nanoparticles,[12–14] and coordination polymers.[15–19] Although the use of different nanodrug delivery systems for cancer drug treatment has achieved encouraging results, the potential biosafety problem still hinders the use of most nanodrug carriers.[20,21] Especially, biodegradability of nanomaterial carriers is a critical challenge in future clinical applications.[22]

The coordination polymer consisting of Fe(III) and gallic acid (GA) has been widely used in drug delivery,[23] in which Fe(III) is coordinated with the –COOH of GA in unsaturated modality.[24,25] It can gradually degrade in response to the weakly acidic tumor microenvironment (TME),[26] and be effectively excreted from the body without causing long-term retention and toxicity problems.[27] Until now, many examples of various drugs have been successfully delivered by the Fe–GA coordination polymer.[28] However, most reported drug loadings by the Fe–GA coordination polymer relied on surface adsorption between the drug molecules and Fe–GA, resulting in unsatisfactory drug loading amount.[29] Therefore, there is an urgent need to design Fe–GA complexes with a larger inner cavity for drug-loaded cancer treatment.

In the meantime, the development of drug-loaded nanomaterials that can be combined with multiple treatment methods is the current trend in cancer therapy. Among the various treatment systems studied in recent years, photothermal therapy (PTT) employs laser light inducing high temperature at tumor sites to kill cancer cells,[30–34] which has higher specificity, minimal invasiveness, and lower side effects. Chemodynamic therapy (CDT) is an emerging treatment strategy that uses chemical reactions such as the Fenton reaction to produce reactive oxygen species (ROS) to kill tumor cells in the tumor *in situ* with minor side effects.[7,35] It uses the iron-catalyzed Fenton reaction to convert hydrogen peroxide (H_2O_2),[28,36] which is less active, into hydroxyl radicals (·OH) with a significantly more vital oxidizing ability.[37,38] Therefore, drug-delivery treatment combined with PTT and CDT treatments is promising for enhancing cancer therapy efficiency.[39–41]

Herein, Fe–GA coordination polymers with a hollow nanosphere structure were prepared for the first time with bovine

[a]*Department of Chemistry, Analytical Instrumentation Center, 105 North Road of Western Third Ring, Haidian District, Beijing 100048, China. E-mail: tianyang@cnu.edu.cn*

[b]*College of Life Science, Capital Normal University, 105 North Road of Western Third Ring, Haidian District, Beijing 100048, China*

† Electronic supplementary information (ESI) available. See DOI: 10.1039/d1na00721a

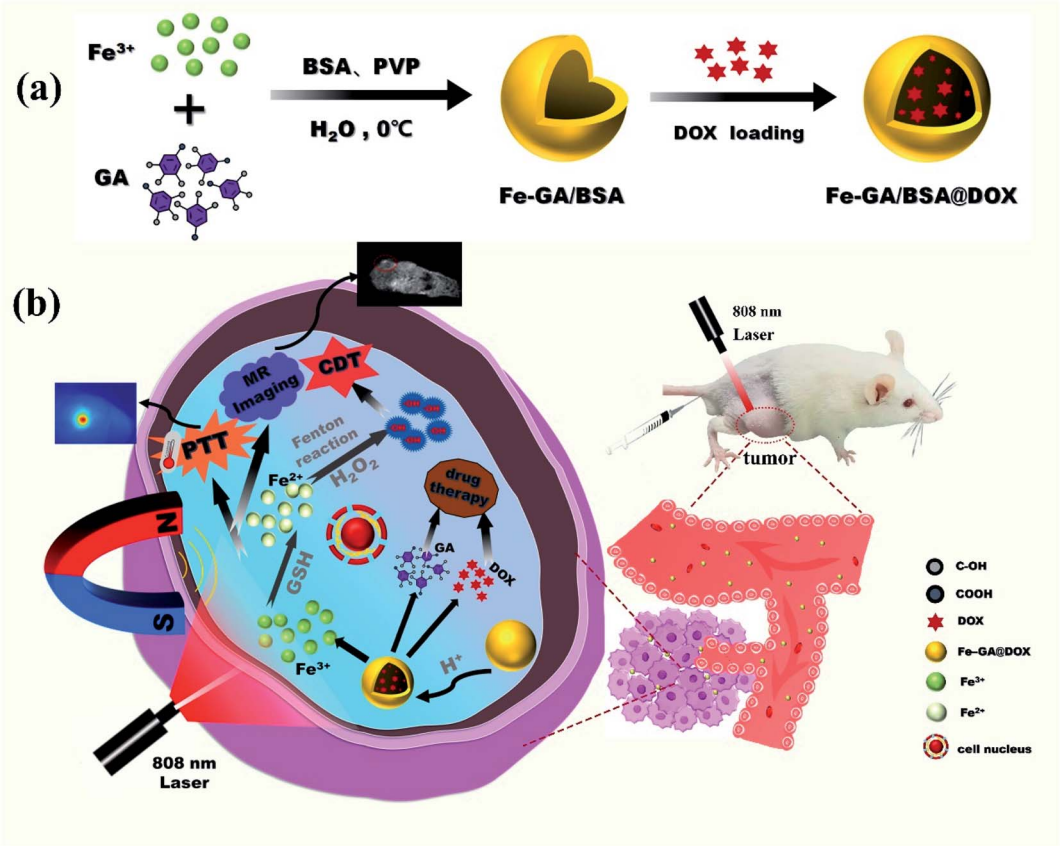

Scheme 1 The procedure of synthesis of hollow Fe–GA/BSA nanospheres and of loading DOX drug into it (a); schematic illustration for the combination therapy of PTT, CDT, and drugs toward tumor with MR imaging for diagnosis (b).

serum albumin (BSA) combination (denoted as Fe–GA/BSA) under mild reaction conditions. With the help of this hollow structure, the drug doxorubicin (DOX) for cancer treatment was physically embedded in the hollow Fe–GA/BSA. The prepared Fe–GA/BSA@DOX would be destroyed due to the unsaturated coordination structure in TME, releasing the drug DOX and Fe(III). The released Fe(III) was reduced by glutathione (GSH) into Fe(II) in TME and reacted with H_2O_2 to generate hydroxyl radicals (·OH) *via* the Fenton reaction for tumor CDT. Furthermore, the Fe–GA/BSA@DOX showed an excellent photothermal conversion effect and could kill cancer cells through PTT. In addition, the Fe–GA/BSA@DOX material also had a noticeable MRI biological imaging effect due to the existence of Fe element. All the above biological synergistic therapy and imaging diagnosis were evaluated by experiments *in vitro* and *in vivo*, suggesting the prepared hollow Fe–GA/BSA nanospheres as a potential image-guided synergistic therapy material, which can realize the integration of diagnosis and treatment (Scheme 1).

2. Results and discussion

2.1 Synthesis and characterization of Fe–GA/BSA@DOX nanospheres

In the synthesis of hollow nanospheres of Fe–GA/BSA coordination polymer, $FeCl_3 \cdot 6H_2O$ and GA were chosen as the precursors and PVP as the surfactant template of the hollow structure; BSA was added in the reaction solution to increase the biocompatibility of the product (details in the ESI†). To obtain high-quality hollow nanospheres, we explored the reaction conditions, such as temperature, reaction time, and surfactant content as shown in Fig. S1 and S2.† Finally, high-quality Fe–GA/BSA hollow nanospheres with uniform size were obtained at 0 °C in 2 h.

The prepared Fe–GA/BSA product was observed by TEM, which indicated that the hollow spherical structure had a diameter of about 200 nm and uniform shell thickness, as shown in Fig. 1a. Energy dispersive X-ray (EDX) spectrum (Fig. 1b) demonstrates the existence of Fe in the hollow spheres and the elements C, N, and S, which came from the GA ligand and BSA molecules. Fig. 1c is the FT-IR spectrum analysis of the prepared Fe–GA/BSA hollow nanospheres. It reveals that the O–H stretching vibration peak of Fe–GA/BSA at 3369 cm^{-1} disappeared, indicating the chelation of the phenols in GA with Fe(III). In addition, the BSA-amide I band vibration at 1650 cm^{-1} and the amide II band vibration at 1521 cm^{-1} suggest that BSA was present in the Fe–GA/BSA hollow nanospheres.

To study the drug delivery of the prepared hollow Fe–GA/BSA nanospheres, we employed a chemotherapeutic drug (DOX) with anticancer effects as the drug model in our work. A 6 mL PBS solution of Fe–GA/BSA (7 mg) was mixed with DOX solution

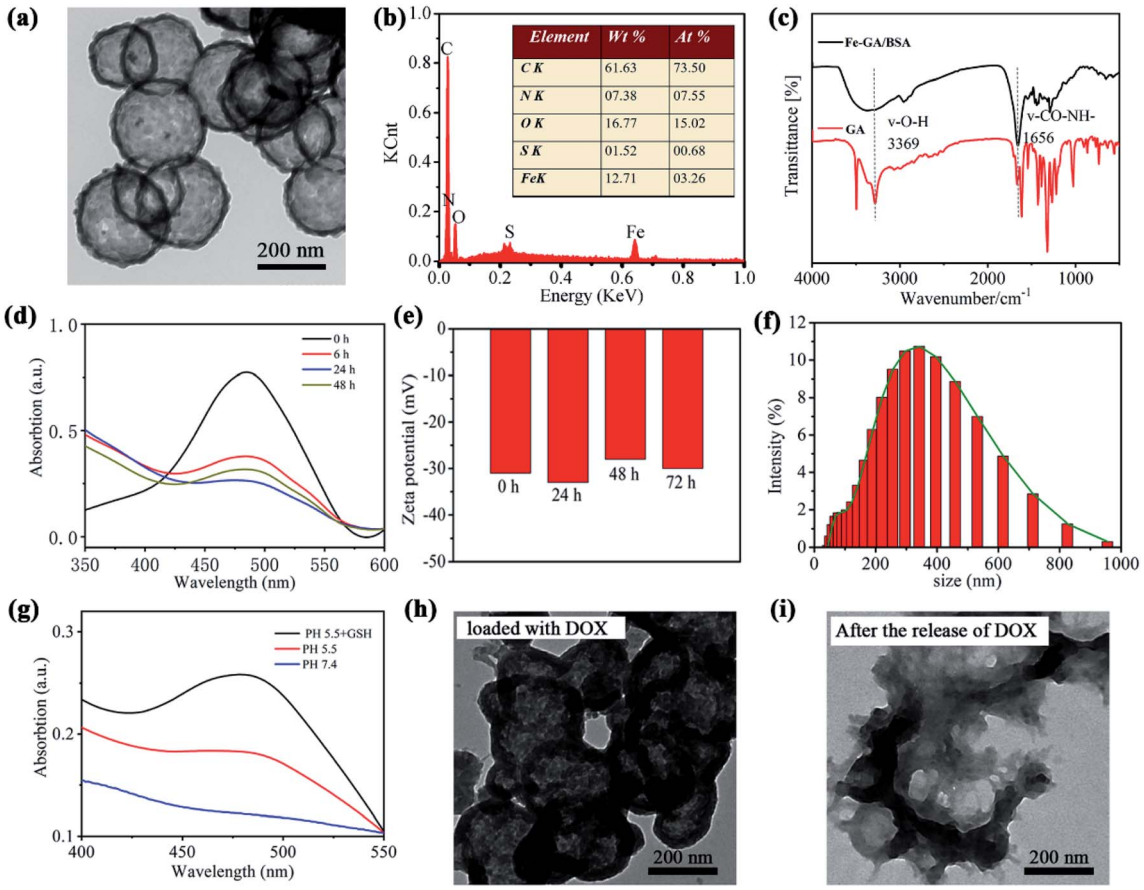

Fig. 1 Characterizations of the Fe–GA/BSA@DOX nanospheres. TEM images (a); EDX spectrum with the inset showing the percentage of elements (b); corresponding IR spectra of the GA and Fe–GA/BSA (c); UV absorption spectra of Fe–GA/BSA loading DOX for different times (d); zeta potential (e) and hydraulic dynamic size of the Fe–GA/BSA@DOX in PBS (pH = 7.4) (f); UV absorption spectra of the solution with drug release under different conditions (g); TEM image of the prepared Fe–GA/BSA hollow spheres with DOX loading (h) and after DOX release (i).

(1.5 mg, 0.25 mg mL^{-1}), and the supernatant was monitored by UV-vis absorption at different time points. As shown in Fig. 1d, the DOX concentration of the supernatant decreased approximately to 48.8% at 6 h, indicating that 51.2% DOX had been loaded in the hollow Fe–GA/BSA nanospheres. The loading of the drug DOX reached the maximal value of 66.1% at 24 h according to UV-vis absorption. Therefore, we characterized the prepared hollow Fe–GA/BSA spheres with DOX loading for 24 h (defined as Fe–GA/BSA@DOX) for further therapy applications. To verify the stabilization in water, the *Z* potential and hydraulic dynamic size of the Fe–GA/BSA@DOX were measured. Fig. 1e shows around −30 mV during the tested 72 h, indicating high surface negative-electricity and satisfactory stabilization in aqueous solution. Simultaneously, the hydraulic dynamic size was distributed around 300 nm, as shown in Fig. 1f.[42]

Subsequently, we studied the Fe–GA/BSA@DOX to verify its targeted release performance in a simulated tumor microenvironment by UV-vis means. Fig. 1g shows that after the sample stayed in a weak alkaline PBS solution (pH = 7.4) for 24 h, its supernatant did not present the absorption peak of DOX. In contrast, after the sample stayed in a weakly acidic PBS solution (pH = 5.5) for 24 h, its supernatant indicated apparent characteristic absorption of DOX around 480 nm. The result suggested well that the Fe–GA/BSA@DOX release the drug for efficient tumor targeting due to the weakly acidic TME. Moreover, it is known that a high expression of GSH in TME is the characteristic of tumor. Therefore, we additionally tested the drug release performance of the Fe–GA/BSA@ DOX in a PBS solution containing GSH at pH 5.5. It shows a significantly enhanced DOX content as shown in Fig. 1g, demonstrating the higher release efficiency in the presence of GSH. This should be attributed to the reduction of Fe(III) by GSH, promoting the degradation of Fe–GA/BSA unsaturated-coordination polymer. The results indicate that the prepared material can be used as a drug delivery nanodrug, with a perfect targeted drug-release performance toward TME.

2.2 Photothermal performances of the Fe–GA/BSA@DOX coordination polymer

To preliminarily test the photothermal performance of the hollow Fe–GA/BSA nanodrugs, we conducted a series of photothermal conversion experiments by using 808 nm laser irradiation (0.7 W cm^{-2}) and used an infrared thermal imager to

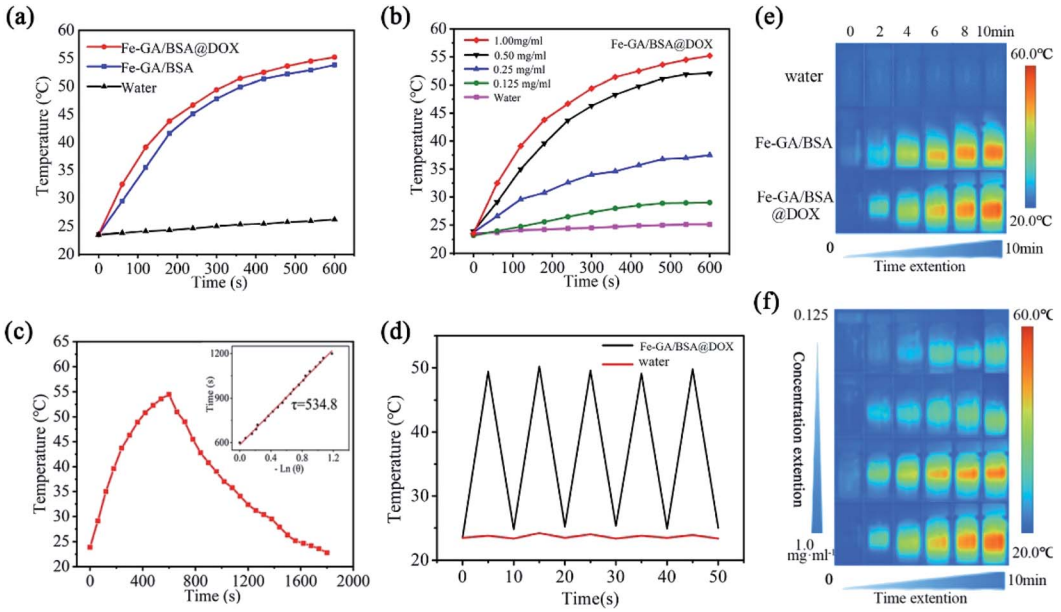

Fig. 2 PTT properties of the Fe–GA/BSA@DOX in an aqueous solution. Photothermal heating temperature curves of different samples against time (a); photothermal heating temperature curves with different concentrations of Fe–GA/BSA@DOX *versus* time (b); photothermal temperature variation of the Fe–GA/BSA@DOX, during which the irradiation was stopped at 10 min (c); and the inset is a plot of cooling time against the negative natural logarithm of the temperature driving force; temperature variation during five cycles of photothermal heating of water and Fe–GA/BSA@DOX (d); photothermal photos of different samples after irradiation (e); photothermal photos of different concentrations of Fe–GA/BSA@DOX after irradiation (f).

monitor the temperature changes. Fig. 2a presents the temperature of pure water raised by about 3 °C (from 23 to 26 °C) after 808 nm laser irradiation for 10 min. In contrast, the solutions containing Fe–GA/BSA or Fe–GA/BSA@ DOX with the concentration of 1 mg mL^{-1} increased to above 50 °C from room temperature, indicating palpable photothermal performance, and the loading of the drug has no negative effect on the photothermal conversion. Fig. 2b shows that the temperature rise is well dependent on the solution concentration of Fe–GA/BSA@DOX from 0 to 1.0 mg mL^{-1}, confirming that the photothermal performance came from the prepared nanodrugs indeed. According to Fig. 2c, the calculated photothermal conversion efficiency of Fe–GA/BSA@DOX is approximately 67.14% (details are provided in the ESI†).[43] Compared with most iron-based photothermal nanodrugs, the prepared Fe–GA/BSA@DOX has a higher photothermal conversion efficiency (Table S2†).[44–49] Furthermore, the prepared Fe–GA/BSA@DOX indicated favorable photothermal performance stability after 5 tested cycles (Fig. 2d). Fig. 2e and f display the color images of the irradiated part corresponding to the temperature curves in Fig. 2a and b, respectively. These results indicate that the Fe–GA/BSA@DOX nanodrug can effectively convert NIR light to local overheating, which provides a possibility for further application in the photothermal therapy of tumors *in vivo*.

2.3 ROS generation of the hollow Fe– GA/BSA nanospheres for CDT

To confirm our deduction that the hollow Fe–GA/BSA nanospheres could play a potential role in CDT for cancer, we simulated the process of producing ˙OH through the Fenton reaction and examined it in an aqueous solution. As a control, the GSH mixed with DOX in PBS (pH = 5.5) rarely decreased and the oxidized GSSG did not increase, which were monitored using the GSH test kit (Fig. S7†). In contrast, as shown in Fig. 3a, the GSH percentage decreased gradually in the PBS (pH = 5.5) solution of the hollow Fe–GA/BSA nanospheres, and reduced to 33% after 5 hours. Correspondingly, the oxidation product of GSH (GSSG), increased from 0 to 81%. The results indicated that the GSH was oxidized by Fe(III) in Fe–GA/BSA, which was accordingly reduced into Fe(II). The produced Fe(II) was further able to catalyze the Fenton reaction in the presence of H_2O_2. Furthermore, as shown in Fig. 3b, a strong ROS signal of ˙OH radicals was detected by ESR analysis, confirming that the hollow Fe–GA/BSA nanospheres could be used for enhanced CDT toward the tumor.

2.4 *In vitro* experiments of the prepared Fe–GA/BSA@DOX

To test the possibility of medical application of the prepared Fe–GA/BSA@DOX, we used the standard 3-(4,5-dimethylthiazol-2-yl)-2,5-diphenyltetrazolium bromide (MTT) method to determine the cell toxicity *in vitro*. In our work, 293 cells (a human renal epithelial cell line), HKC cells (a human renal tubular epithelial cell line), HeLa cells (a human epithelioid cervix carcinoma cell line), C6 cells (rat glioma cells), and Pc-12 cells (pheochromocytoma cells of the rat adrenal medulla) were incubated respectively with the Fe–GA/BSA@DOX of various concentrations (0–500 μg mL^{-1}) for 12 h and 24 h. As shown in Fig. 4a and b, the cell viability of 293 cells and HKC cells was not only retained up to 90% after 12 h of incubation but also up to 80% with 24 h of incubation. The results demonstrated that the Fe–GA/BSA@DOX

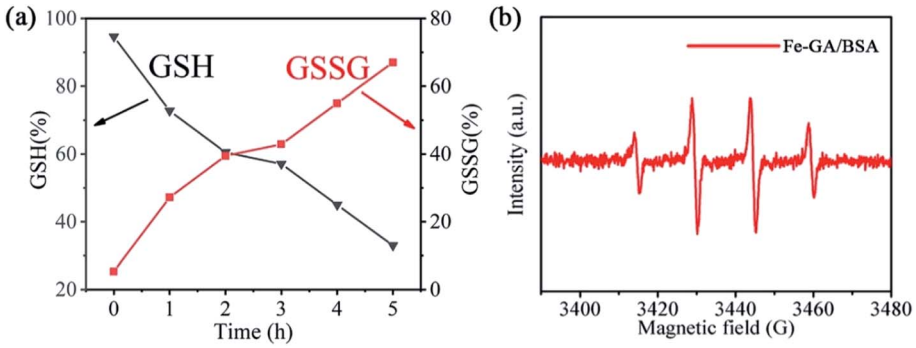

Fig. 3 Characterizations of the hollow Fe–GA/BSA nanospheres for CDT in aqueous solution. Detection of GSH and GSSG in the mixed solution of Fe–GA/BSA and GSH (a); ESR spectrum of Fe–GA/BSA with the capture of ·OH (b).

nanodrug was less destructive and highly biologically safe to normal cells. However, Fig. 4c–e showed that the three kinds of cancer cells suffered palpable damage at the Fe–GA/BSA@DOX concentration of 500 μg mL^{-1}. Especially, the viability of the incubated C6 cells was preserved less than 80% only at 125 μg mL^{-1} Fe–GA/BSA@DOX after 12 hours and decreased to less than

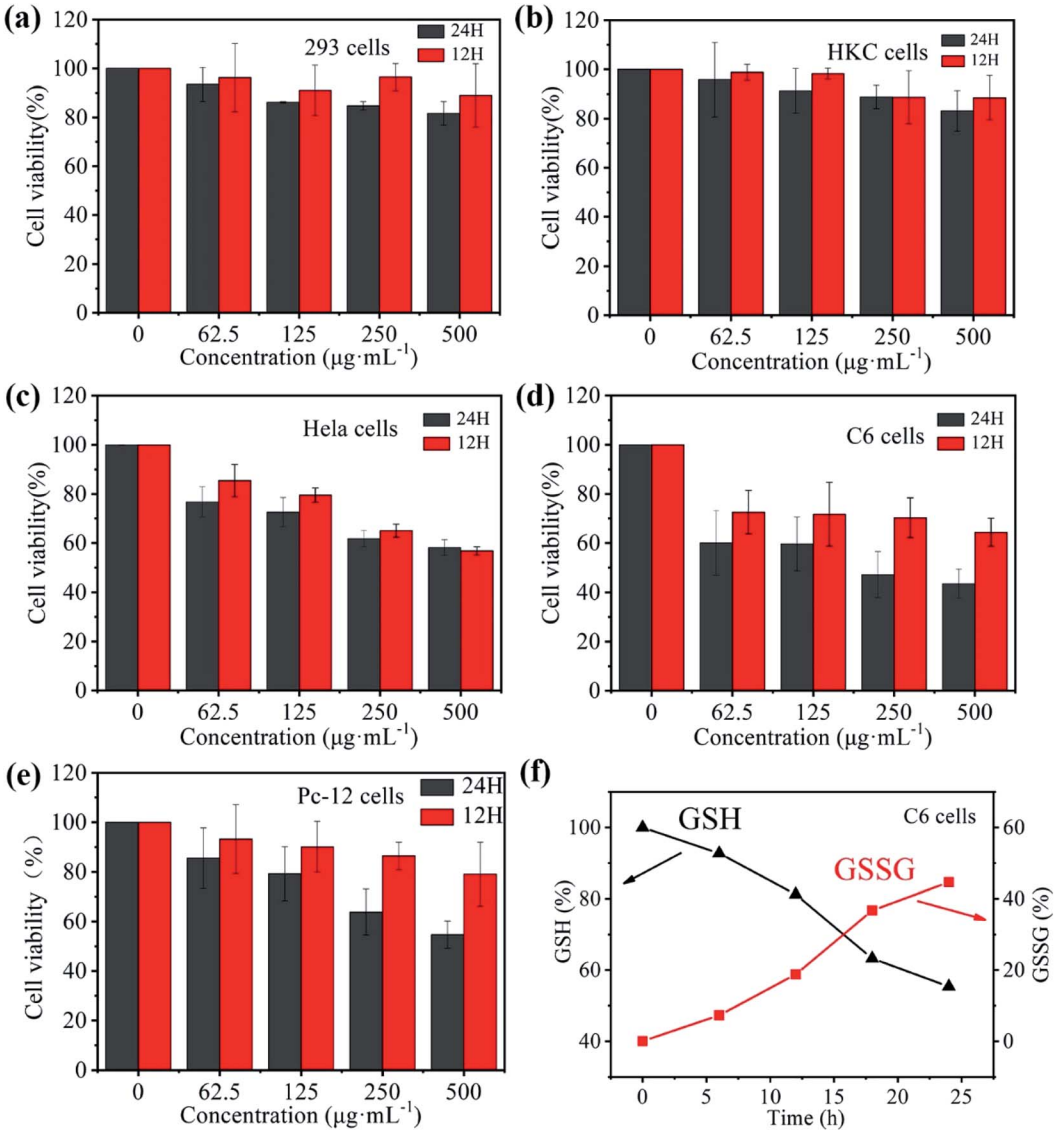

Fig. 4 Cell viability diagrams of the cells treated with different concentrations of Fe–GA/BSA@DOX in the culture for 12 and 24 hours: 293 cell lines (a); HKC cell lines (b); HeLa cell line (c); C6 cell line (d); Pc-12 cell line (e). Detection of GSH and GSSG in C6 cells (f).

60% in 24 h of incubation. This confirmed that the prepared nanodrug could lead to the apoptosis of tumor cells. Further study showed that (Fig. 4f) the GSH in C6 cells was consumed obviously, which decreased *ca.* 50%; the oxidation product GSSG of GSH increased from 0 to 50% correspondingly. All results indicated that the released DOX in cancer cells and CDT effects caused by the Fenton reaction in the TME were responsible for cancer cell apoptosis.

2.5 *In vivo* PTT and MRI performances of the prepared nanodrugs

Inspired by the excellent photothermal conversion efficiency *in vitro*, we studied the PTT efficiency of the Fe–GA/BSA@DOX *in vivo*. All animal procedures were performed in accordance with the Guidelines for Care and Use of Laboratory Animals of Capital Normal University and experiments were approved by the Animal Ethics Committee of Capital Normal University. To obtain a tumor mouse model, approximately 10^6 individual glioma cells were injected subcutaneously into male CD-1 experimental mice (6 weeks old, weighing 20–25 g) for 7 days of feeding. Then the glioma-bearing mice (tumor volume ~100 mm^3) were injected with 200 μL PBS, Fe–GA/BSA (1 mg mL^{-1}), and Fe–GA/BSA@DOX (1 mg mL^{-1}) solutions, respectively. Following this, an NIR laser with the wavelength of 808 nm (0.7 W cm^{-2}) was used to irradiate mouse tumors for 10 min. During the irradiation, the temperature change data and photothermal photos of the tumor site were obtained through an NIR thermal imager. Fig. 5a is a thermal image of the whole body of a mouse taken at different time intervals. The results showed that under NIR irradiation, the temperature of the tumor site increased rapidly after the injection of Fe–GA/BSA and Fe–GA/BSA@DOX. In contrast, the mice injected with PBS detected a minimal temperature increase under NIR radiation. As shown in Fig. 5b, under NIR laser irradiation, the temperature of the tumor area containing Fe–GA/BSA or Fe–GA/BSA@DOX increased rapidly to above 60 °C within 10 minutes. The high temperature above 60 °C is sufficient to kill cancer cells, suggesting that the prepared hollow nanospheres are favorable for the PTT of the tumor.

Based on the excellent performance of previous MRI tests *in vitro* (Fig. S8†), 200 μL Fe–GA/BSA@DOX in PBS solution (1 mg mL^{-1}) was administered intravenously to the glioma-bearing mice at the dose of 10 mg kg^{-1}. MRI system (0.47 T) was used to detect and record T_1 and T_2 signals before and after injection at various time points. Fig. 5c shows the T_1-weighted MR images of the mouse with post-injection of Fe–GA/BSA@DOX from 0 h to 24 h. Before the injection (or at 0 h), the MR image of the tumor site showed considerable darkness (Fig. 5c). With the increase of time, the tumor area gradually changed from dark to bright, indicating the imaging effect of a representative T_1 contrast agent. It displayed the brightest signal after the post-injection of 5 hours. Then, the T_1-weighted image became dark gradually again, indicating the beneficial metabolic effect in the mouse body. On the other hand, Fig. 5d shows the T_2-weighted images of the mouse for post-injection of the Fe–GA/BSA@DOX from 0 h to 24 h. The MR image of the tumor site showed considerable brightness before the injection (or at 0 h); then, the T_2-weight images changed from bright to dark, which showed that the material had the imaging effect of a representative T_2 contrast agent. The T_2 signal of the tumor site reached the maximal value after the post-injection of 5 h. At the same time, the tumor site in Fig. 5d returned to bright after post-injection of 24 hours, also proving that the prepared Fe–GA/BSA@DOX had good metabolism and low toxicity.

2.6 *In vivo* combination therapy of PTT, CDT, and drug treatment

We further studied the combination therapy efficiency of the Fe–GA/BSA@DOX *in vivo via* the glioma-bearing mouse model.

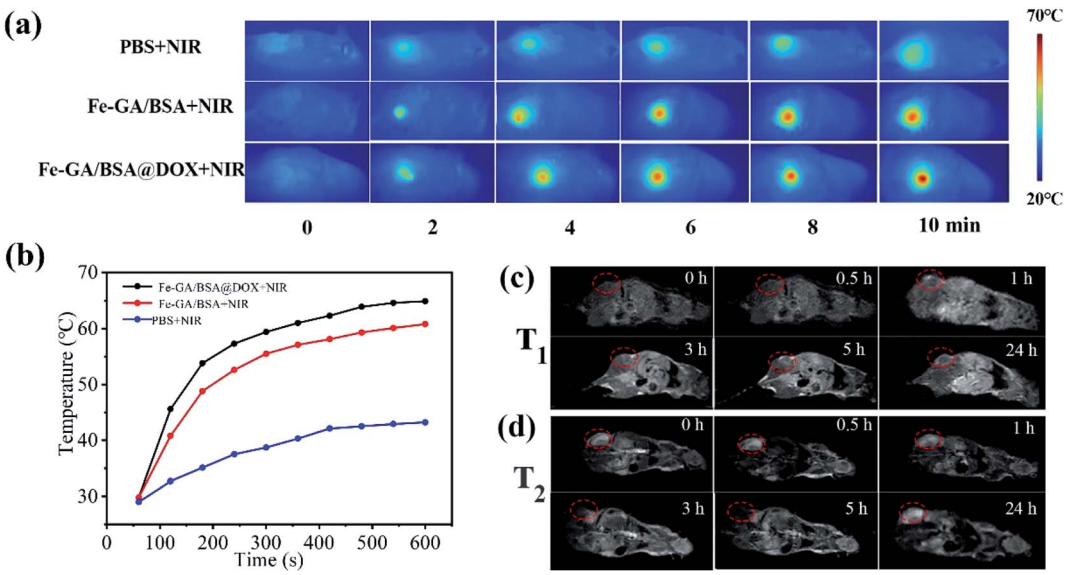

Fig. 5 The NIR thermal images of a tumor-bearing mouse with various injections for PTT (a); the temperature curve corresponding to the tumor site with various injections (b); T_1- (c) and T_2-weighted (d) MRI images for the tumor-bearing mouse depending on time.

When the volume of the solid tumor grew to ~100 mm^3, we randomly divided the glioma-bearing mice into six groups for different treatments, including (1) only PBS (control group), (2) only hollow Fe–GA/BSA nanospheres, (3) Fe–GA/BSA@DOX, (4) PBS + NIR laser irradiation (10 minutes, 0.7 W cm^{-2}), (5) Fe–GA/BSA + NIR laser irradiation (10 minutes, 0.7 W cm^{-2}), and (6) Fe–GA/BSA@DOX + NIR laser irradiation (10 minutes, 0.7 W cm^{-2}). The injection doses of the used PBS, Fe–GA/BSA (1 mg mL^{-1}), and Fe–GA/BSA@DOX (1 mg mL^{-1}) solution were 200 μL, which were all injected through the tail vein of the mice.

After the next 20 days of injection, we recorded the growth of subcutaneous tumors in mice with different treatments. We took pictures of the tumors for each treated mouse every 4 days (Fig. 6a) and recorded the tumor volume every 2 days (Fig. 6b). As shown in Fig. 6a and b, the PBS group had no obvious antitumor effect on the mice in the monitored 20 days without NIR radiation. However, the Fe–GA/BSA group tumor dwindled gradually, and the tumor volume approached 0 on the 20th day. This suggests that the hollow Fe–GA/BSA nanospheres worked CDT against the tumor efficiently because the Fe ions catalyzed the Fenton reaction to produce ROS of ·OH. In addition, the Fe–GA/BSA@DOX group showed that the tumor volume depressed quickly in 10 days, and the tumor nearly vanished on the 18th day. This result demonstrated that the anticancer drug DOX delivered by Fe–GA/BSA could accelerate the tumor treatment.

On the other hand, NIR irradiation of 808 nm was further applied to the tumor-bearing mice with injections of PBS, Fe–GA/BSA (1 mg mL^{-1}), and Fe–GA/BSA@DOX (1 mg mL^{-1}), respectively. As suggested in Fig. 6a and b, the tumor growth was hardly blocked in the PBS + NIR group. However, the tumors in the Fe–GA/BSA + NIR group and Fe–GA/BSA@DOX + NIR group clearly showed a scab, indicating the PTT effect of the prepared hollow Fe–GA/BSA nanospheres. Significantly, the tumor growth in the Fe–GA/BSA@DOX + NIR group was rapidly inhibited after 2 days of NIR irradiation, which was shorter than that of Fe–GA/BSA + NIR (4 days). All results show that the Fe–GA/BSA@DOX + NIR group had the most substantial antitumor effect due to the combination treatment of PTT, drugs, and CDT. Moreover, no recurrence was detected within the next two months.

At the same time, Fig. 6c showed that the bodyweight of each group kept increasing, and the mice survival-rate was 100%, proving that our combined treatment had fewer side effects. Finally, the experimental mice were sacrificed after the observation of 20 days, and the possibility of toxicity to major organs was studied by hematoxylin and eosin staining (Fig. S10†). No obvious tissue abnormalities or damage was found in the mice's heart, liver, spleen, lung, and kidney in all groups, which indicated that the Fe–GA/BSA@DOX has no apparent systemic toxicity to major organs during tumor treatment. All

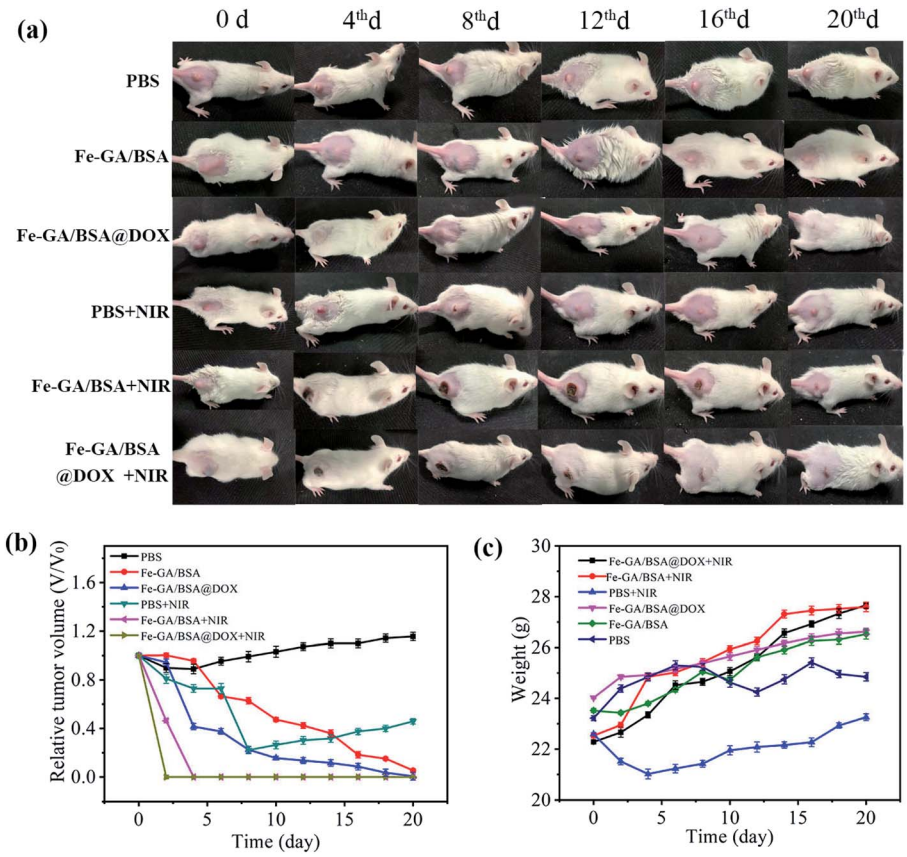

Fig. 6 Representative photos of tumor-bearing mice with various treatments at different days (a); relative tumor volume curve of the tumor-bearing mice corresponding to various treatments, where the relative tumor volume was normalized to the initial size (b); the bodyweight of the mice in the six groups after various treatments *versus* different times (c).

experimental results showed that the Fe–GA/BSA@DOX has excellent tumor inhibitory effects *via* drug delivery, PTT, and CDT with good biocompatibility and minimal side effects.

3. Conclusion

In summary, we prepared hollow Fe–GA/BSA nanospheres as a framework for drug delivery of DOX. The Fe–GA/BSA@DOX could be disrupted, leading to the nanospheres' cleavage and thus releasing the DOX encapsulated inside for drug treatment of tumor tissues. At the same time, the released Fe(III) consumed the overexpressed GSH in tumor cells to obtain Fe(II), which triggered the Fenton reaction to produce $^{\bullet}$OH. The hydroxyl radicals can kill tumor cells in the CDT of cancer. In addition, the Fe–GA/BSA@DOX showed a high photothermal conversion efficiency of 67.14%, making it an excellent agent of PTT. Meanwhile, this material can also be used as a T1 and T2 contrast agent. Overall, the Fe–GA/BSA@DOX has achieved the simultaneous action of three therapies (drug therapy, PTT, and CDT) and cancer diagnosis. We expect that this therapeutic strategy will provide new insights into the future of cancer treatment.

Conflicts of interest

There are no conflicts to declare.

Acknowledgements

This work is financially supported by the National Natural Science Foundation of China (No. 52172096) and classification development at Capital Normal University (No. 2155091, 2155160, 2155161).

References

1 R. van der Meel, E. Sulheim, Y. Shi, F. Kiessling, W. J. Mulder and T. Lammers, *Nat. Nanotechnol.*, 2019, **14**, 1007–1017.
2 R. G. Kenny and C. Marmion, *Chem. Rev.*, 2019, **119**, 1058–1137.
3 J. Shi, P. W. Kantoff, R. Wooster and O. C. Farokhzad, *Nat. Rev. Cancer*, 2017, **17**, 20–37.
4 I. de Lázaro and D. J. Mooney, *Nat. Mater.*, 2021, 1–11.
5 R. Kumari, D. Sunil and R. Ningthoujam, *J. Controlled Release*, 2019, **319**, 135–136.
6 Y. Bae and K. Park, *Adv. Drug Delivery Rev.*, 2020, **158**, 4–16.
7 C. Liu, Y. Cao, Y. Cheng, D. Wang, T. Xu, L. Su, X. Zhang and H. Dong, *Nat. Commun.*, 2020, **11**, 1–9.
8 A. Shetty and S. Chandra, *Mater. Today Chem.*, 2020, **18**, 100381.
9 N. Fernandes, C. F. Rodrigues, A. Moreira and I. Correia, *Biomater. Sci.*, 2020, **8**, 2990–3020.
10 Y.-f. Zhang, F. Fang, L. Li and J. Zhang, *ACS Biomater. Sci. Eng.*, 2020, **6**, 4816–4833.
11 H. Yin, P. Cao, X.-Y. Wang, Y. Li and X. Yin, *Computed Tomography Imaging-Guided Tandem Catalysis-Enhanced Photodynamic Therapy with Gold Nanoparticle Functional Covalent Organic Polymers*, 2020, pp. 2534–2542.
12 H. J. Won, B. Ryplida, S.-G. Kim, G. Lee, J. Ryu and S. Y. Park, *ACS Nano*, 2020, **14**, 8409–8420.
13 Y. Xiao, Y. Gu, L. Qin, L. Chen, X. Chen, W. Cui, F. Li, N. Xiang and X. He, *Colloids Surf., B*, 2021, **200**, 111581.
14 C. Wang, N. Zhao and W. Yuan, *ACS Appl. Mater. Interfaces*, 2020, **12**, 9118–9131.
15 Y. Liu, S. Lv, D. Liu and F. Song, *Acta Biomater.*, 2020, **116**, 16–31.
16 X. Li, S. Lu, X. Mu, T. Li, S. Sun, Y. Zhao, J. Hai and B. Wang, *Biosens. Bioelectron.*, 2021, **190**, 113417.
17 W. Meng, J. Hao, Z. Tong, H. Liu, Y. Li and X. Zhang, *Inorg. Chim. Acta*, 2020, 120108.
18 L. Ni, S.-L. Wang, J. Zhao, G. Wu and L.-Y. Lang, *J. Mol. Struct.*, 2020, **1227**, 129364.
19 X. Yu, T. Jin, F. Lu, Z.-J. Luo, C. Liu and W.-X. Jin, *Arabian J. Chem.*, 2021, **14**, 102998.
20 Y. Wang, Z. Li and Q. Hu, *Nano Today*, 2021, **38**, 101127.
21 Z. Liao, S. W. Wong, H. L. Yeo and Y. Zhao, *NanoImpact*, 2020, **20**, 100253.
22 W. Wang, X. Liu, X. Zheng, H. Jin and X. Li, *Adv. Healthcare Mater.*, 2020, **9**, e2001117.
23 H. Zheng, B. Ma, Y. Shi, Q. Dai, D. Li, E. Ren, J. Zhu, J. Liu, H. Chen, Z. Yin, C. Chu, X. Wang and G. Liu, *Chem. Eng. J.*, 2021, **406**, 126888.
24 X. Mu, C. Yan, Q. Tian, J. Lin and S. Yang, *Int. J. Nanomed.*, 2017, **12**, 7207.
25 Q. Tian, Y. Cai, N. Li, Q. Liu, B. Gu, Z.-G. Chen and S. Song, *Nanomedicine*, 2020, **28**, 102219.
26 P. Zhang, Y. Hou, J. Zeng, Y. Li, Z. Wang, R. Zhu, T. Ma and M. Gao, *Angew. Chem., Int. Ed.*, 2019, **58**, 2–11.
27 C. Zhang, J. Li, C. Yang, S. Gong, H. Jiang, M. Sun and C. Qian, *Nanomedicine*, 2020, **23**, 102071.
28 E. Hwang and H. S. Jung, *Chem. Commun.*, 2020, **56**, 8332–8341.
29 K. Han, W. Y. Zhang, J. Zhang, Z. Y. Ma and H. Y. Han, *Adv. Healthcare Mater.*, 2017, **6**, 1700470.
30 Y. Liu, P. Bhattarai, Z. Dai and X. Chen, *Chem. Soc. Rev.*, 2019, **48**, 2053–2108.
31 Q. Chen, Q. Hu, E. Dukhovlinova, G. Chen, S. Ahn, C. Wang, E. A. Ogunnaike, F. S. Ligler, G. Dotti and Z. Gu, *Adv. Mater.*, 2019, **31**, 1900192.
32 X. Li, J. Lovell, J. Yoon and X. Chen, *Nat. Rev. Clin. Oncol.*, 2020, **17**, 1–18.
33 S. Liu, X. Pan and H. Liu, *Angew. Chem.*, 2020, **132**, 5943–5953.
34 Z. Zhang, D. Ni, F. Wang, X. Yin, S. Goel, L. N. German, Y. Wang, J. Li, W. Cai and X. Wang, *Nano Res.*, 2020, **13**, 3217–3223.
35 Q. Tian, F. Xue, Y. Wang, Y. Cheng, L. An, S. Yang, X. Chen and G. Huang, *Nano Today*, 2021, **39**, 101162.
36 X. Liu, Y. Jin, T. Liu, S. Yang, M. Zhou, W. Wang and H. Yu, *ACS Biomater. Sci. Eng.*, 2020, **6**, 4834–4845.
37 S. Gao, Y. Jin, K. Ge, Z. Li, H. Liu, X. Dai, Y. Zhang, S. Chen, X. Liang and J. Zhang, *Adv. Sci.*, 2019, **6**, 1902137.

38 Z. Tang, Y. Liu, M. He and W. Bu, *Angew. Chem., Int. Ed.*, 2019, **58**, 946–956.
39 Y. Shi, J. Zhang, H. Huang, C. Cao, J. Yin, W. Xu, W. Wang, X. Song, Y. Zhang and X. Dong, *Adv. Healthcare Mater.*, 2020, **9**, 2000005.
40 X. Wang, X. Zhong, Z. Liu and L. Cheng, *Nano Today*, 2020, **35**, 100946.
41 Y. Cheng, H. Lu, F. Yang, Y. Zhang and H. Dong, *Nanoscale*, 2021, **13**, 3049–3060.
42 Y. Wang, Y. Wu, Y. Liu, J. Shen, L. Lv, L. Li, L. Yang, J. Zeng, Y. Wang and L. W. Zhang, *Adv. Funct. Mater.*, 2016, **26**, 5335–5344.
43 Q. Tian, J. Hu, Y. Zhu, R. Zou, Z. Chen, S. Yang, R. Li, Q. Su, Y. Han and X. Liu, *J. Am. Chem. Soc.*, 2013, **135**, 8571–8577.
44 L.-S. Lin, Z.-X. Cong, J.-B. Cao, K.-M. Ke, Q.-L. Peng, J. Gao, H.-H. Yang, G. Liu and X. Chen, *ACS Nano*, 2014, **8**, 3876–3883.
45 Y. Liu, S. Liu, C. Hu, Y. Li and M. Pang, *Dalton Trans.*, 2019, **48**, 16848–16852.
46 Y. Wang, X. Liu, G. Deng, Q. Wang, L. Zhang, Q. Wang and J. Lu, *J. Mater. Chem. B*, 2017, **5**, 4221–4232.
47 S. Zhou, X. Jiao, Y. Jiang, Y. Zhao, P. Xue, Y. Liu and J. Liu, *Appl. Surf. Sci.*, 2021, **552**, 149498.
48 Y. Meng, J. Yang, R. Jiang, S. Wang, L. Zheng, G. Wang, X. Tian, H. Zhu, D. Yan and C. Liu, *Appl. Surf. Sci.*, 2021, **562**, 150189.
49 J. Wang, H. Zhao, Z. Zhou, P. Zhou, Y. Yan, M. Wang, H. Yang, Y.-j. Zhang and S. Yang, *ACS Appl. Mater. Interfaces*, 2016, **8 31**, 19872–19882.